



Nano Synthesis and Characterization of Co and Mn Co-doped ZnO by Solution Combustion Technique

Elavarthi Pragna¹ · Mangiri Ramanadha² · Ande Sudharani² · Kummara Sunil Kumar²

Received: 19 January 2021 / Accepted: 23 March 2021 / Published online: 1 April 2021

© The Author(s), under exclusive licence to Springer Science+Business Media, LLC, part of Springer Nature 2021

Abstract

Pure zinc oxide (ZnO) and Co and Mn co-doped ZnO nanoparticles were synthesized via a solution combustion technique. Structural, compositional, morphological, functional, optical, magnetization, and photoluminescence properties were examined. X-ray diffraction studies confirmed the hexagonal structure, and the average crystallite size of the synthesized samples was found to be around 20 to 30 nm. From the SEM analysis, all synthesized samples were spherical. Energy dispersion spectra confirm the presence of all selective elements in the synthesized samples. From UV-Vis spectra, we observed that there is decrease in band gap with increase in Co/Mn concentration. From photoluminescence (PL) studies, a decrease in the rate of recombination of electron-hole pair generation is observed. Experiments carried out using vibrating sample magnetometer studies revealed magnetic properties that indicate ferromagnetism in synthesized samples at room temperature. This material offers enormous potential to develop spintronics and optoelectronic materials due to its low cost and good yield.

Keywords ZnO · Co and Mn co-doped ZnO nanoparticles · XRD · Magnetization · PL

1 Introduction

Semiconductor (SC) nano-materials have garnered increasing research activity because of their unique physical and chemical properties and their ability to control their size, shape, and composition over a wide range [1–3]. ZnO has been recognized as a promising host nano-material for doping of transition metals (TM) (TM = Zn, Cd, Fe, Mn, Cu, Cr, etc.) at room temperature (RT). Recently, significant advances have been made in the study of metal oxide (M-O) co-doped M-O (i.e., ZnO) nanomaterials based on both basic research and pioneering advanced technologies [4]. RT ferromagnetic materials have been successfully synthesized by several groups. ZnO have gained intense attention in searching for high Curie temperature (T_C) ferromagnetic diluted magnetic semiconductors (DMS) materials, which are based on ZnO. Since DMS could exhibit ferromagnetism above RT upon doping with

transition metal elements [5]. ZnO with a wide bandgap of 3.37 eV and a high excitation binding energy (60 meV) was an attractive MOSC (metal oxide semiconductor) material [6].

ZnO crystallizes in two primary forms, hexagonal wurtzite and cubic zincblende. Under normal room temperature and pressure, ZnO has a hexagonal wurtzite structure. The zincblende ZnO structure can be stabilized only by growth by using specific conditions [7]. ZnO crystalline nature could be indexed to known hexagonal ZnO systems with $a = b = 0.32498$ nm and $c = 0.52066$ nm. The c/a ratio is 1.633 which is the ideal value for a hexagonal cell [8]. The adaptation of the chemical, physical, and functional properties of ZnO size and shape offers enormous potential for many technological uses [9]. The synthesis of ZnO nano-materials has received a lot of attention because of the growing interest in size-dependent properties and applications such as light-emitting diodes, lasers, nanogenerators, electronics, spintronics, gas sensor, biosensor, cosmetics, storage, optical devices, window materials for displays, solar cells, drug-delivery, and photocatalysts [10–14]. As a result, various manufacturing routes have been proposed to synthesize ZnO-based nanomaterials with morphologies and scales adapted from micro to nano to enhance their performance [15].

Extensive investigations have been carried out on ZnO-doped TM systems which were produced using various

✉ Kummara Sunil Kumar
seelaiah786@gmail.com

¹ Department of Mechanical Engineering, Indian Institute of Technology (BHU), Varanasi 221005, India

² Department of Physics, Sri Venkateswara University, Tirupati 517502, India

methods like sol-gel technique, hydrothermal method, co-precipitation method, flame spray pyrolysis technique, solvothermal method, ultrasonic dispersion, boiling method, solution combustion technique (SCT), chemical deposition technique, thermal decomposition method, solid-state technique, microwave method, etc. [16–19]. SCT reaction was occurring or formed with evolution of heat (of a chemical reaction or compound). The SCT process is an excellent technique for the production of nanoscale ZnO. This process is swift, reliable, requires inexpensive raw materials, does not require high-temperature furnaces, and can produce any oxide material. Several researchers have produced ZnO nanoparticles using the SCT method and studied the structural and optical properties of the synthesized ZnO [20].

Recently, many researchers have claimed that ferromagnetism can be obtained at room temperature in pure non-magnetic metal oxide nanoparticles and that ferromagnetic properties do not depend on the dopant of the transition metal. TM ions are also doped to ZnO, and we expected that TM's 3d electrons would improve the electrical, optical, and magnetic properties of ZnO [21]. Other studies confirm that TM ions can alter the properties of ZnO. Dinesha et al. reported that Co/Fe co-doped ZnO nanoparticles made by SCT are best suited for ferrofluid and magnetic recording applications [22]. Gao et al. noted that Mn-doped ZnO nanoparticles made by the co-precipitation process are best suited for ferromagnetic applications [23]. Sharma et al. reported that Fe/Co-doped ZnO nanoparticles made by the co-precipitation process are best suited for photoluminescence and spintronic applications [24]. Papadaki et al. reported that TM (Cu, Mn, and Co) doped ZnO nanoparticles prepared by a microwave-friendly process are best suited for photocatalytic applications [25]. Belkhaoui et al. reported that Mn-doped ZnO nanoparticles made by the co-precipitation process are best suited for radio frequency applications [26]. Sharma et al. noted that Co/Mn co-doped ZnO nanoparticles made by the co-precipitation process are best suited for spintronic and optoelectronic applications (Co constant and Mn varied) [27]. Pazhanivelu et al. reported that Co-doped ZnO:Mn nanoparticles made by the co-precipitation process are best suited for ferromagnetic applications [28]. Kumar et al. noted that Mn-doped ZnO nanoparticles made by SCT are best suited for photocatalytic applications [29]. Yasoda et al. reports that Cu-doped ZnO:Mn nanoparticles made by SCT are best suited for photoluminescence and spintronics applications [30].

Also, an ounce of literature was available on SCT synthesis in a solution of pure ZnO and nanoparticles doped with various metal ions (TM, RE, and AE). Few reports are available on Co-doped ZnO:Mn nanoparticles by different routes [27, 28], but there is few report on Co-doped ZnO:Mn nanoparticles synthesized using SCT method, and this work aims to improve scope of magnetization and photoluminescence studies. In this article, we discussed XRD, SEM, EDS, FTIR, UV-

Vis absorption, VSM, and PL studies on Co-doped ZnO:Mn nanoparticles.

2 Materials Method and Characterization Techniques

2.1 Materials Method

Pure ZnO and Co and Mn co-doped ZnO (Mn = 2% and Co = 0, 1, 2%) nanoparticles were synthesized by SCT method. Zinc nitrate hexahydrate ($\text{Zn}(\text{NO}_3)_2 \cdot 6\text{H}_2\text{O}$), cobalt nitrate hexahydrate ($\text{Co}(\text{NO}_3)_2 \cdot 6\text{H}_2\text{O}$), manganese acetate tetrahydrate ($\text{Mn}(\text{CH}_3\text{COO})_2 \cdot 4\text{H}_2\text{O}$), urea ($\text{CO}(\text{NH}_2)_2$), polyethylene glycol (PEG-400) ammonium (NH_3) solution was used as a starting material, all chemicals were purchased from Sigma-Aldrich and Hi-Media and used without further purification. Zinc nitrate and urea were dissolved each in 40 ml of deionized water separately with a molar ratio of 1:5. Zinc nitrate and urea were taken in grams based on molecular weight (MW) in proportion to the molarity that is zinc molarity one and urea molarity 5. Co and Mn were also taken with molar concentration of zinc with respect to the percentage. (Co and Mn doping element percentages increases and Zn element percentage decreases).

Each liquid stirred for 30 min, and then urea solution was added drop wise to the zinc nitrate solution and stirred for 30 min. Next, an ammonia solution was added drop wise to the above-mixed solution until the pH became 9, and the solution became white, after that 2 ml of PEG solution was added to the above solution, and stirring was continued for 7 h. Finally, the solution was stored in a closed muffle furnace at a combustion temperature of 500 °C for 1 h (INDFURR SUPERHEAT FURNACES (maximum temperature level up to 1000 °C)) [30]. The dopant Mn concentration was adjusted to 2% due to the improved magnetization and the slow rate of recombination of electron-hole pair to synthesize ZnO:Mn (2%) and Co and Mn co-doped ZnO (Co = 2 % and 4%) samples using a similar method. All synthesized samples were tempered at 600 °C for 1 h. All samples were labeled as pure ZnO (ZnO-0), ZnO:Mn (2%) (ZnO-1), and Co-doped ZnO:Mn (Co = 2% and Co 4%) (ZnO-2 and ZnO-3) respectively.

2.2 Characterization Techniques

The synthesized samples were exposed to various properties. An X-ray diffractometer (XRD) was used to determine the crystal structure of synthesized samples with Cu-K α radiation ($\lambda = 0.154$ nm) (Benchtop Powder X-ray Diffraction (XRD) Instrument (Rigaku Company)). Surface morphology, compositional analysis, and particle size were analyzed using a scanning electron microscope (SEM) attached with energy

dispersive X-ray analysis (EDAX) (ZEISS EVO MA-15). Fourier transform infrared (FTIR) spectra were recorded on a Thermo Nicolet 6700 spectrophotometer, and the optical properties were characterized using a UV-Vis absorption spectrometer (Varian: 5000). The magnetization hysteresis loop (M-H loop) was evaluated at room temperature using a vibrating sample magnetometer (VSM) (Lakeshore: 7410) with a fluorescence spectrometer (FluoroLog-FL3-11) using Xe lamp (400 W) at an excitation wavelength of 425 nm.

3 Results and Discussion

3.1 Structural Analysis

The crystalline structure and orientation of the synthesized nanoparticles were studied by the X-ray diffraction (XRD) method. The XRD patterns of ZnO-0, ZnO-1, ZnO-2, and ZnO-3 nanoparticles are shown in Fig. 1a and b, and the calculated parameters are shown in Table 1. The broad and intense peaks indicate that the samples are crystalline and that the ZnO nanoparticles are in nanoform. From the XRD spectra, three firm prominent diffraction peaks appearing at 31.8°, 34.3°, and 36.3° correspond to the (100), (002), and (101) planes of the ZnO hexagonal structure, respectively (JCPDS database card number 05-0664). All samples have a preferred orientation along the plane (101) [31, 32]. However, in addition to dominant ZnO peaks, comparatively less intense peaks corresponding to secondary phases of Co are observed in the case of Co and Mn co-doped ZnO nanoparticle [33]. From Fig. 1b, it can be seen that there is a slight clear shift to the side of the higher 2θ in samples of ZnO-1, and lower 2θ in the sample of ZnO-2, and ZnO-3 at around 36° in compared with ZnO-0, indicates the incorporation of Co/Mn into the Zn site of ZnO. The incorporation of Co and Mn ions seems to have noticeable impact on the crystal structure of the ZnO. Besides this, it is worth mentioning that some of these diffraction peaks becomes weaker as dopant concentration changes. This change in intensity is accompanied by a very small shift towards higher angles in the broad peaks of co-doped ZnO nanoparticles with reference to the ZnO. The shift in the position of the peak to higher angles as a result of co-doping may

be explained by the contraction of the lattice parameters due to the size difference between the Zn atoms and the dopants atoms [34–36]. The shift may be due to the lower ionic radii of Co/Mn compared with Zn. This type of shift has also been observed in PL, UV-Vis absorbance, and FTIR studies.

From Debye–Scherrer’s formula:

$$D = \frac{K\lambda}{\beta \cos\theta}$$

where *K* is the Scherrer’s constant (*K* = 0.9 for spherical symmetry), λ is the wavelength of the XRD radiation used (λ = 0.154 nm), θ represents the Bragg angle and β is the half-full width height (FWHM) [37].

Formulae for lattice parameters:

$$a = \frac{\lambda}{\sqrt{3} \sin\theta},$$

$$c = \frac{\lambda}{\sin\theta}$$

here *a* = *b* and *c* are the lattice parameters [38].

The average size of crystallites is found to be around 36 nm for ZnO-0 nanoparticles. The average crystallite size for the ZnO-1, ZnO-2, and ZnO-3 samples is approximately 26, 29, and 32 nm, respectively. It is seen that, compared to ZnO-1, in Co/Mn-doped samples of ZnO-2 and ZnO-3 there is a slight increase in the size of the crystallites. The slight increase in the crystallite’s size could be due to the reduction of point defects and the rearrangement of the crystal grain. The decrease in point defects may be due to Co/Mn’s lower solubility in the ZnO material. The results obtained are very much in agreement with previous reports. Jayakumar et al. reported similar structural parameters in Co/Mn-doped ZnO samples [39]. The XRD patterns of the Co/Mn co-doped ZnO nanoparticles are identical to those of ZnO. Co and Mn’s influence on ZnO is low due to the low concentration of dopant [40].

3.2 Morphology and Compositional Analysis

Figure 2 shows the surface morphology of the synthesized nanoparticles of ZnO-0, ZnO-1, ZnO-2, and ZnO-3 by SCT. SEM micrographs indicate that all prepared samples consist of

Table 1 Crystallographic parameters information of ZnO and Co and Mn co-doped ZnO nanoparticles

S. no.	Sample	Lattice parameters		Crystallite size (<i>D</i>) (nm)	Strain	Volume (<i>V</i>) (Å) ³
		<i>a</i> = <i>b</i> (nm)	<i>c</i> (nm)			
1	ZnO-0	0.3254	0.5213	36.28	0.0032	47.80
2	ZnO-1	0.3240	0.5204	26.71	0.0029	47.31
3	ZnO-2	0.3242	0.5209	29.58	0.0039	47.41
4	ZnO-3	0.3248	0.5211	32.92	0.0034	47.61

Fig. 1 **a** XRD spectra of ZnO and Co and Mn co-doped ZnO nanoparticles and **b** enlarged view of XRD spectra at 36°

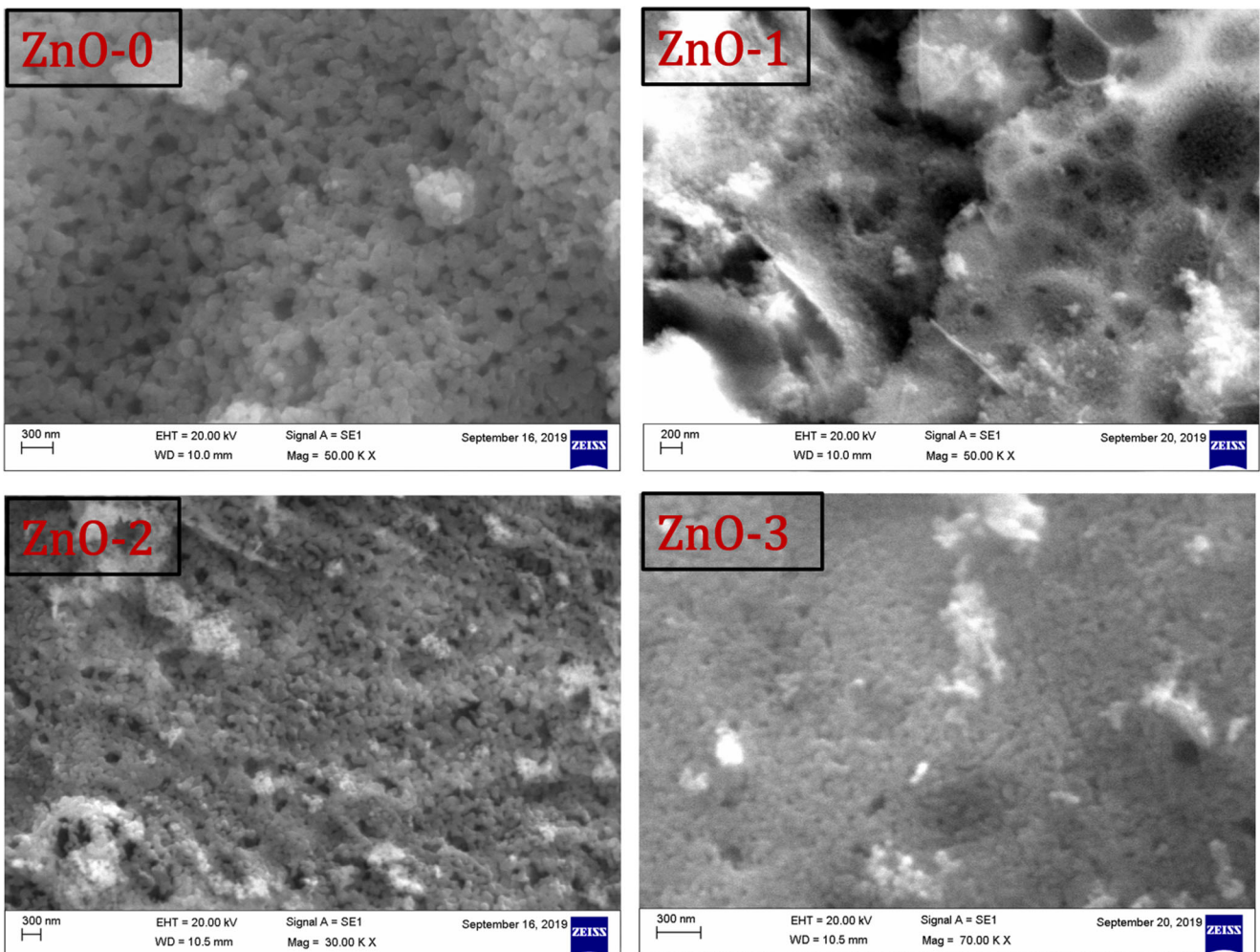
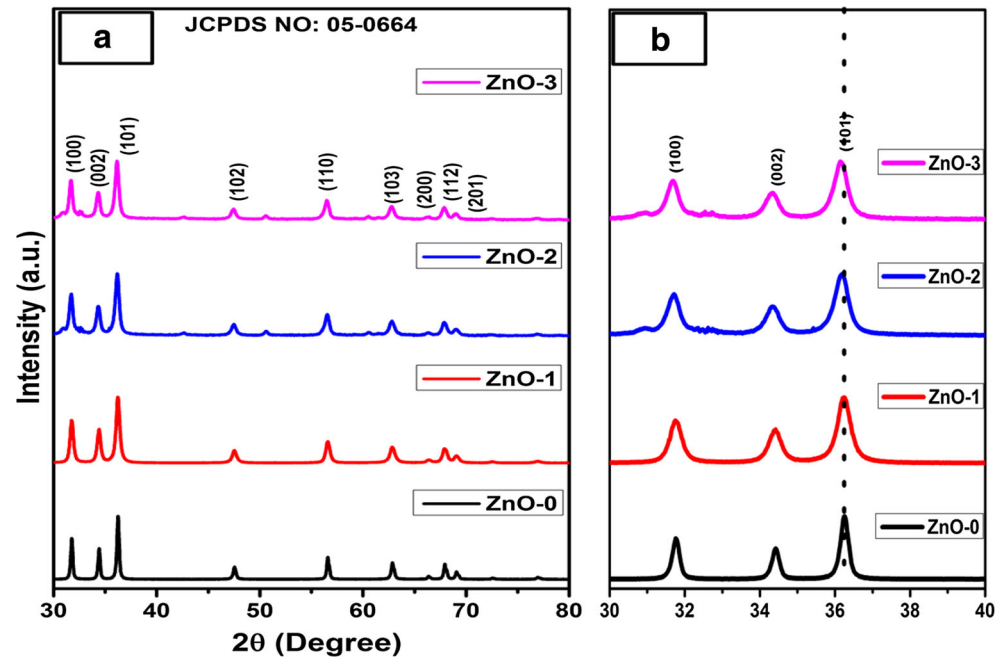


Fig. 2 SEM micrographs of ZnO and Co and Mn co-doped ZnO nanoparticles

nanoscale particle aggregations. The morphology of particles in all the synthesized samples is spherical with a smaller size and a more homogeneous size distribution. In Mn-doped samples, the particle size decreased markedly in ZnO-1, whereas in the co-doping concentration of Co/Mn samples, it increased slightly in ZnO-2 and ZnO-3.

EDS is used to detect the presence of target compositions in prepared samples. Figure 3 shows the EDS spectra of nanoparticles of ZnO-0, ZnO-1, ZnO-2, and ZnO-3 by SCT. The EDS spectrum confirms that all the selective elements of Zn, Mn, Co, and O were present and that the compositions of the synthesized samples were in an almost stoichiometric ratio. The elemental compositions of the prepared samples are shown in Table 2. All samples exhibited homogeneous constituents of the elements regardless of the selected areas in the samples. Furthermore, the EDS results confirmed that the prepared samples are free of impurities.

3.3 FTIR Analysis

FTIR spectroscopic analysis provides qualitative and quantitative information on chemical compounds (both organic and inorganic) and detects their functional groups, as well as information on covalent bonds. Figure 4 shows the FTIR spectra of nanoparticles of ZnO-0, ZnO-1, ZnO-2, and ZnO-3 at room temperature in the range of 400 to 4000 cm^{-1} . Prominent bands are seen at approximately 450 cm^{-1} due to stretching vibration of the Zn–O (metal-oxy) bond in tetrahedral coordination. At about 671–672 cm^{-1} , fragile bands arise from stretching vibrations of Zn–O bonds in octahedral arrays. The Zn–O bonds at the co-tetrahedral co-band frequencies at 1380 cm^{-1} are attributed to the C=O group’s asymmetric stretching vibrations. Vibrating bands at approximately 1650 cm^{-1} are assigned to the C=O group [41, 42].

The band frequencies of approximately 2346 cm^{-1} are due to the CO₂ molecules present in the atmospheric air. The band around 2910 cm^{-1} and 2925–2926 cm^{-1} is reflected due to bending of the C–H bond and stretching of the C–H bond, respectively. These bands show the presence of absorbed groups on the surface of the nanocrystals. The large absorption peaks of approximately 3420 cm^{-1} are attributed to the

hydroxyl group (OH) due to H₂O. It represents the existence of water molecules adsorbed on the surface of the nanocrystals [43]. Co/Mn-doped ZnO nanocrystals can quickly disperse in non-polar and polar solvents due to the hydroxyl groups on the surface. These surface hydroxyl groups help provide functional groups that can react with functional organic molecules. All functional groups were assigned to synthesized samples. In the graph, the absorption band at approximately 450 cm^{-1} is seen to shifting slightly, indicating the incorporation of Mn and Co/Mn ions into the Zn site of ZnO material. This type of change exhibits the structural parameters and optical bandgap and is correlated with the XRD, PL, and UV-Vis absorption studies.

3.4 Optical Studies

Figure 5 shows the UV-Vis spectra of nanoparticles of ZnO-0, ZnO-1, ZnO-2, and ZnO-3 at room temperature in the range of 300 to 480 nm. All samples exhibited a strong absorption edge in the 350 to 400 nm wavelength range, denoting the prepared nanoparticle’s potentiality for photoluminescence properties. The incorporation of Co/Mn ions into the Zn site of ZnO improved the absorption rate compared to the ZnO-0 sample [44, 45]. The lower absorption edge observed at the intrinsic frontal absorption edge in the wavelength range around 330–390 nm may be due to the “sp-d” exchange interactions between the band electrons and the localized “d” electrons; the Co²⁺/Mn²⁺ ions can cause the band structure to change. The forbidden optical band (E_g) is determined from Tauc formulas [30]

$$(\alpha h\nu)^2 = A(h\nu - E_g)$$

where $h\nu$ is the photon’s energy in eV, α is the absorption coefficient, and A is the material-dependent constant. E_g is evaluated from the intersection of the graph $(\alpha h\nu)^2$ with respect to $h\nu$, as shown in Fig. 6. The values of E_g calculated are in the range of 3.368 to 3.033 eV (Table 3). In the doped samples (ZnO-1 and ZnO-2), the E_g values decrease slightly with the doping of Mn and increases for Mn/Co ions ZnO-0, the rise in the absorption intensity in the blue region may also be due to a more pronounced doping concentration of ZnO with the manganese ion. Ullah and Dutta [46] reported that the improvement in optical absorption of Mn-doped ZnO samples is due to the increase in defect sites in the crystal structure compared to ZnO. ZnO doping with Co²⁺/Mn²⁺ adds a tail state in the valence band’s vicinity due to defect sites reduces its sufficient bandgap. Therefore, visible light’s energy will be enough to excite electrons from the tail state to the conduction state. In the ZnO-3 samples, the increase in the optical bandgap for the Co/Mn-co-doped ZnO samples is interpreted as “4s-3d” and “2p-3d” exchange interactions that are

Table 2 Compositional analysis of ZnO and Co and Mn co-doped ZnO nanoparticles

S. no.	Sample	Elemental compositions (at.%)				Total
		Zn	Mn	Co	O	
1	ZnO-0	79.87	–	–	20.13	100
2	ZnO-1	77.75	2.09	–	20.16	100
3	ZnO-2	75.97	2.06	2.04	19.93	100
4	ZnO-3	73.77	2.2	3.94	20.09	100

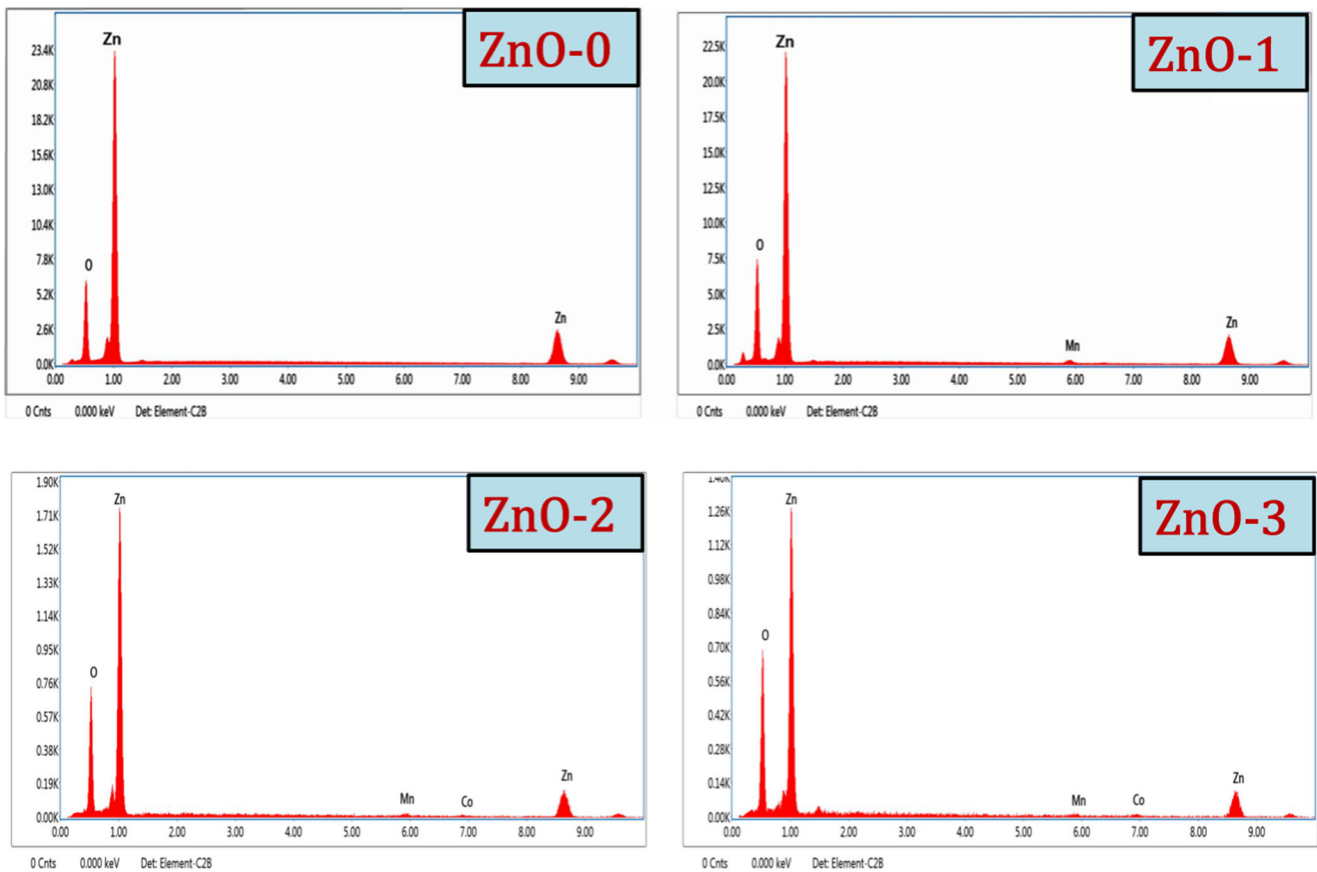


Fig. 3 EDS of ZnO and Co and Mn co-doped ZnO nanoparticles

responsible for the decrease in “3d” electron density of Zn and the increase in electron density “3d” Mn below the maxima of

the valence band [47]. The widening of the optical bandgap with Co/Mn elbow in the ZnO sample may also be due to the Burstein-Moss band’s filling effect.

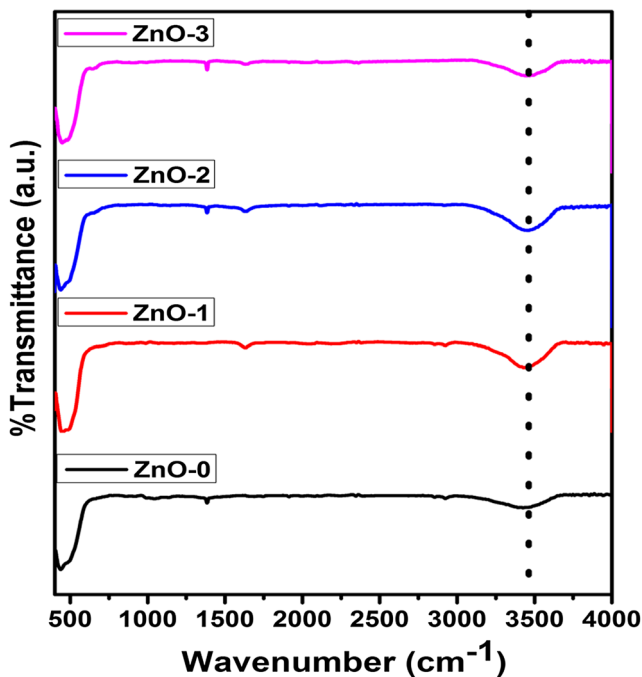


Fig. 4 FTIR spectra of ZnO and Co and Mn co-doped ZnO nanoparticles

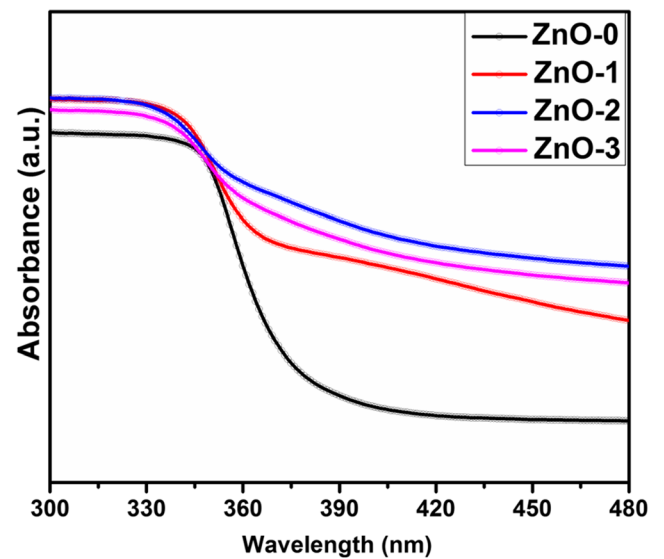


Fig. 5 UV-Vis absorption spectra of ZnO and Co and Mn co-doped ZnO nanoparticles

Table 3 Optical band gap values of ZnO and Co and Mn co-doped ZnO nanoparticles.

S. no.	Sample	Eg (eV)
1	ZnO-0	3.368
2	ZnO-1	3.328
3	ZnO-2	3.033
4	ZnO-3	3.181

Table 4 Magnetization parameters of ZnO and Co and Mn co-doped ZnO nanoparticles

S. no.	Sample	M_S (emu/g)	M_R (emu/g)	H_C (G)
1	ZnO-0	0.008	0.0021	56.49
2	ZnO-1	0.032	0.0051	168.44
3	ZnO-2	0.126	0.0056	66.289
4	ZnO-3	0.108	0.0078	63.568

3.5 Magnetization Studies

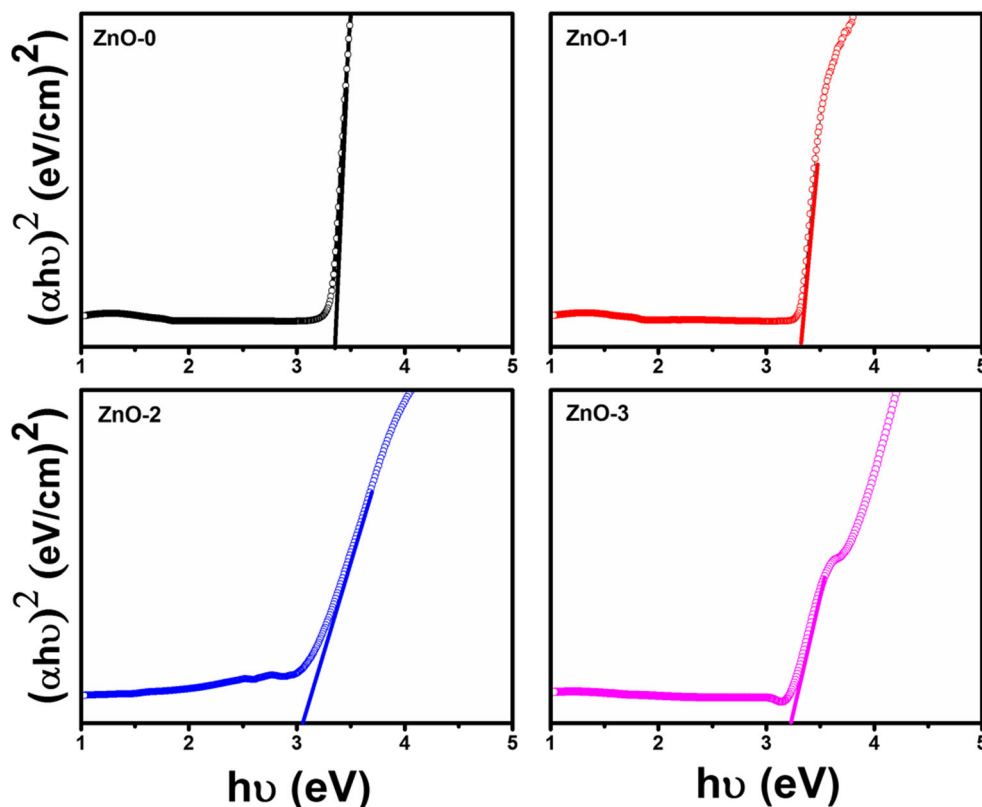
The M-H hysteresis loop of the synthesized samples was recorded using a vibrating sample magnetometer (VSM) at room temperature. Figure 7 shows the M-H hysteresis loop of ZnO-0, ZnO-1, ZnO-2, and ZnO-3 recorded at room temperature. In the ZnO sample, ferromagnetism should be strongly influenced by the nanoparticles’ size, shape, and surface/volume ratio. Nanoparticles with a high surface/volume ratio can have ferromagnetic-related defects [48]. From the figure, it is seen that all samples exhibited a ferromagnetic nature of exchange interactions; the magnetization parameters (saturation magnetization (M_S) and remanent magnetization (M_R)) also increase with increasing doping concentration relative to the ZnO sample and were noted in Table 4.

Since Co/Mn doping on ZnO nanoparticles is hopelessly diluted, direct interaction between magnetic ions is not

possible for the double exchange mechanism. As shown in the PL spectrum, Co/Mn-doped ZnO nanoparticles consist of vacant zinc defects and oxygen-related defects. Furthermore, an intrinsic exchange interaction due to individually ionized oxygen promotes bound magnetic polaron theory (BMP) and improves ferromagnetic properties at room temperature [49]. Therefore, we adopt the BMP mechanism to confirm the evolution of magnetic property in doped nanoparticles. Thus, the improvement in ferromagnetism for the ZnO sample associated with Co/Mn at room temperature is expected to be caused by the higher concentration of vacant oxygen couplings and Co/Mn ions. In contrast, the exchange interaction of the Co^{2+}/Mn^{2+} ions with the electrons trapped in the oxygen vacancies will align the spins of the two doping ions in a parallel configuration [50].

To summarize the magnetic properties, in synthesized nanoparticles, the magnetic property is described as the

Fig. 6 Optical band gap spectra of ZnO and Co and Mn co-doped ZnO nanoparticles



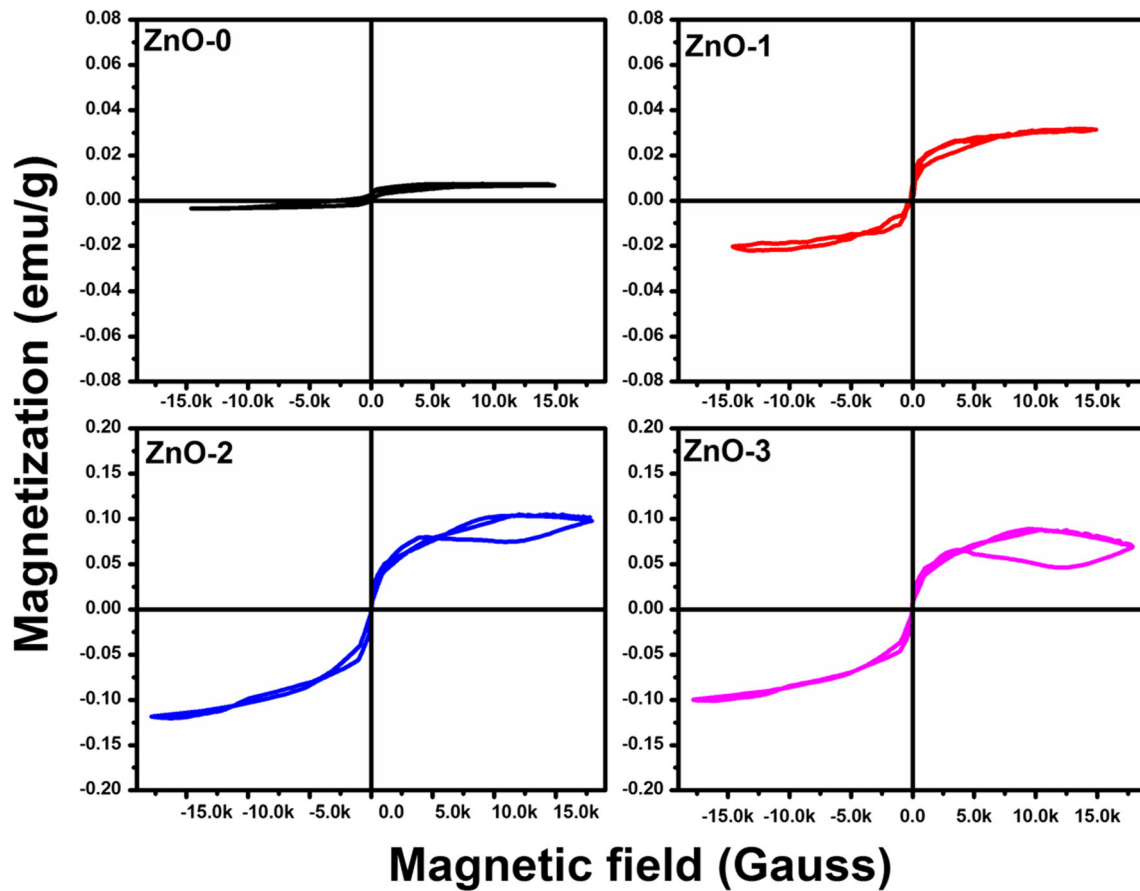


Fig. 7 M-H hysteresis loop of ZnO and Co and Mn co-doped ZnO nanoparticles

localized magnetic moment systems originating from “d” shell electrons of $\text{Co}^{2+}/\text{Mn}^{2+}$ ions located at the sites of the Zn^{2+} lattice. The paramagnetic properties of these systems can be described reasonably well by the efficient Brillouin function, indicating the AFM exchange interactions between the $\text{Co}^{2+}/\text{Mn}^{2+}$ ions [50]. Furthermore, for the ZnO-2 (Co-2% and Mn-2%) sample with the highest Co/Mn ions, an additional loop is observed at high magnetic fields, indicating the first-order phase transitions. The results obtained suggest the use of Co/Mn dopants to improve ZnO’s magnetic properties effectively.

3.6 Photoluminescence (PL) Studies

Figure 8 shows that the PL spectra of ZnO-0, ZnO-1, ZnO-2, and ZnO-3 samples were measured at room temperature with excitation wavelength at 425 nm. The PL emission peaks are broad, probably due to the presence of defects and various recombination sites. Three peaks were observed in the figure at approximately 520 nm, 580 nm, and 700 nm in the spectral region of 500–750 nm [51, 52]. In this figure, in the ZnO-1, ZnO-2, and ZnO-3 samples, their emission intensity decreased gradually compared to the ZnO-0 sample, and that the position of the emission peaks slightly shifted in doped samples

compare to ZnO. In the figure, the emission regions could be interpreted as follows: the green-yellow-orange emissions (520–560 nm and 560–610 nm) could be due to the single absence of charged oxygen (V_o^+) and to the double absence of charged oxygen (V_o^{++}), respectively [23]. Studies by Xu

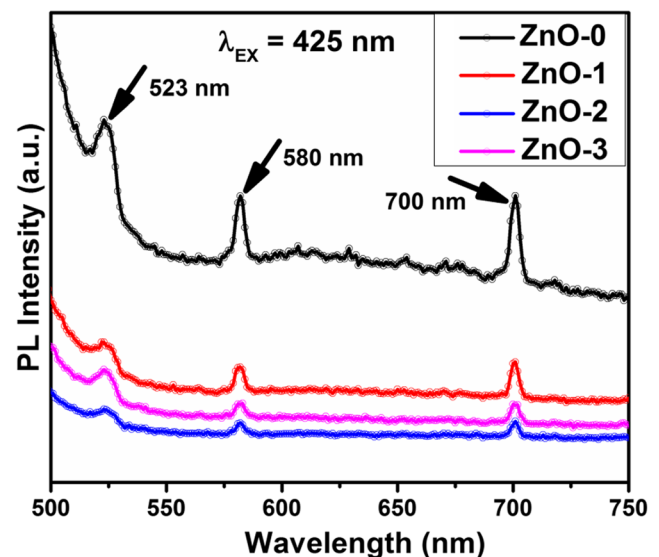


Fig. 8 PL spectra of ZnO and Co and Mn co-doped ZnO nanoparticles

suggest that red emission from 620–690 nm could be attributed to interstitials of oxygen (O_i), from 690–750 nm could have been caused by a lack of oxygen (V_o) [53].

In conclusion, the donor defect is a region of significant deficiencies in the Co/Mn-doped Zn site of ZnO, more electrons can be released, enhancing the generation of oxygen vacancies that improve photoactivity, photodegradation, and photocurrent properties. In our studies results of PL, FTIR, XRD, and UV-Vis absorbance study are consistent with one another.

4 Conclusions

In coda, samples of ZnO-0, ZnO-1, ZnO-2, and ZnO-3 were prepared using the solution combustion technique (SCT), and X-ray diffraction analysis showed that all the samples had a hexagonal wurtzite structure and the particle size decreased in the enriched samples compared to ZnO-0. All the samples were spherical and required elements from SEM and EDS analysis presented in the stoichiometric ratio. The FTIR spectra confirm that all functional groups were present in the prepared samples. According to optical absorption studies, the reduced optical bandgap value in doped samples (ZnO-1, ZnO-2, and ZnO-3) is comparable to ZnO (ZnO-0). The PL measurements showed the emission of red with its wavelength in the range of 620 to 750 nm due to the lack of oxygen (V_o), which is highly dependent on the Co/Mn concentration, and this event is rarely observed. ZnO-2 (Co-2% and Mn-2% (Eg ~ 3.03 eV and D ~ 29nm)) shows the significant improvement in magnetization and can find applications in photoluminescence, spintronics, and optoelectronic devices. Thus, the systematic study of Co/Mn doping's influence on the properties of ZnO can contribute to the advancement of research on spintronic materials.

Acknowledgements This work was financially supported by University Grants Commission under UGC-BSR-RFSMS fellowship scheme (F.25-1/2014-15(BSR)/5-99/2007(BSR)).

References

- Cassee, F.R., Van Balen, E.C., Singh, C., Green, D., Muijsers, H., Weinstein, J., Dreher, K.: *Crit. Rev. Toxicol.* **41**, 213–229 (2011)
- Bundschuh, M., Filser, J., Luderwald, S., Mc Kee, M.S., Metreveli, G., Schaumann, G.E., Schulz, R., Wagner, S.: *Environ. Sci. Eur.* **30**, 1–7 (2018)
- Masala, O., Seshadri, R.: *Annu. Rev. Mater. Res.* **34**, 41–81 (2004)
- Palomino, A.G.: *Physics*. University of Puerto Rico (2006)
- Norberg, N.S., Kittilstved, K.R., Amonette, J.E., Kukkadapu, R.K., Schwartz, D.A., Gamelin, D.R.: *J. Am. Chem. Soc.* **126**, 9387–9398 (2004)

- Zhuang, H., Wang, J., Liu, H., Li, J., Xu, P.: *Acta Phys. Pol. A.* **119**, 819–823 (2011)
- Ashrafi, A.B., Jagadish, C.: *J. Appl. Phys.* **102**, 4 (2007)
- Wang, Z.L., Guo, R., Li, G.R., Ding, L.X., Ou, Y.N., Tong, Y.X.: *RSC Adv.* **1**, 48–51 (2011)
- Gerigk, M., Ehrenreich, P., Wagner, M.R., Wimmer, I., Reparaz, J.S., Torres, C.M., Schmidt-Mende, L., Polarz, S.: *Nanoscale.* **7**, 16969–16982 (2015)
- Park, W.I., Yi, G.C.: *Adv. Mater.* **16**, 87–90 (2004)
- Ong, C.B., Ng, L.Y., Mohammad, A.W.: *Renew. Sust. Energ. Rev.* **81**, 536–551 (2018)
- Djurisic, A.B., Chen, X., Leung, Y.H., Ng, A.M.: *J. Mater. Chem.* **22**, 6526–6535 (2012)
- Kusiak-Nejman, E., Wojnarowicz, J., Morawski, A.W., Narkiewicz, U., Sobczak, K., Gierlotka, S., Lojkowski, W.: *Appl. Surf. Sci.* **541**, 148416 (2021)
- Wang, S., Gao, M., Ma, B., Xi, M., Kong, F.: *Environ. Pollut.* **257**, 113596 (2020)
- El Ghoul, J., Kraini, M., Lemine, O.M., El Mir, L.: *J. Mater. Sci. Mater. Electron.* **26**, 2614–2621 (2015)
- Xu, S., Wang, Z.L.: *Nano Res.* **4**, 1013–1098 (2011)
- Gavrilovic, T.V., Jovanovic, D.J., Dramićanin, M.D.: *Nanomater. Green Energy.* 55–81 (2018)
- Bensebaa, F.: *Interface Sci. Technol.* **19**, 85–146 (2013)
- Wojnarowicz, J., Chudoba, T., Lojkowski, W.: *Nanomaterials.* **10**, 1086 (2020)
- Varma, A., Mukasyan, A.S., Rogachev, A.S., Manukyan, K.V.: *Chem. Rev.* **116**, 14493–14586 (2016)
- Hakeem, A.A.: *J. Magn. Magn. Mater.* **322**, 709–714 (2010)
- Dinesha, M.L., Jayanna, H.S., Mohanty, S., Ravi, S.: *J. Alloys Compd.* **490**, 618–623 (2010)
- Gao, Q., Dai, Y., Li, C., Yang, L., Li, X., Cui, C.: *J. Alloys Compd.* **684**, 669–676 (2016)
- Sharma, D., Jha, R.: *Ceram. Int.* **43**, 8488–8496 (2017)
- Papadaki, D., Mhlongo, G.H., Motaung, D.E., Nkosi, S.S., Panagiotaki, K., Christaki, E., Assimakopoulos, M.N., Papadimitriou, V.C., Rosei, F., Kiriakidis, G., Ray, S.S.: *ACS omega.* **4**, 16429–16440 (2019)
- Belkhaoui, C., Mzabi, N., Smaoui, H.: *Mater. Res. Bull.* **111**, 70–79 (2019)
- Sharma, D., Jha, R.: *J. Alloys Compd.* **698**, 532–538 (2017)
- Pazhanivelu, V., Selvadurai, A.P., Zhao, Y., Thiyagarajan, R., Murugaraj, R.: *Phys. B Condens. Matter.* **481**, 91–96 (2016)
- Kumar, K.A., Amanchi, S.R., Sreedhar, B., Ghosal, P., Subrahmanyam, C.: *RSC Adv.* **7**, 43030–43039 (2017)
- Yasoda, B., Kumar, K.S., Ramanadha, M., Sudharani, A., Vijayalakshmi, R.P.: *J. Supercond. Nov. Magn.* **33**, 1413–1421 (2020)
- Brahma, S., Rao, K.J., Shivashankar, S.: *Bull. Mater. Sci.* **33**, 89–95 (2010)
- Elilarassi, R., Chandrasekaran, G.: *J. Mater. Sci. Mater. Electron.* **21**, 1168–1173 (2010)
- Chanda, A., Gupta, S., Vasundhara, M., Joshi, S.R., Mutta, G.R., Singh, J.: *RSC Adv.* **7**, 50527–50536 (2017)
- Yahmadi, B., Kamoun, O., Alhalaili, B., Alleg, S., Vidu, R., Turki, N.K.: *Nanomaterials.* **10**, 1507 (2020)
- Liu, H., Li, W., Zhang, X., Sun, Y., Song, J., Yang, J., Gao, M., Liu, X.: *Ceram. Int.* **41**, 3613–3617 (2015)
- Voicu, G., Miu, D., Ghitulica, C.D., Jinga, S.I., Nicoara, A.I., Busuioc, C., Holban, A.M.: *Ceram. Int.* **46**, 3904–3911 (2020)
- Sharma, P.K., Dutta, R.K., Pandey, A.C.: *J. Magn. Magn. Mater.* **321**, 4001–4005 (2009)
- Taha, K., M'hamed, M., Idriss, H.: *J. Ovonic Res.* **11**, 271–276 (2015)
- Jayakumar, O.D., Gopalakrishnan, I.K., Kulshreshtha, S.K.: *J. Mater. Chem.* **15**, 3514–3518 (2005)

40. Maensiri, S., Laokul, P., Klinkaewnarong, J., Thomas, C.: *Appl. Phys. A Mater. Sci. Process.* **94**, 601–606 (2009)
41. Muthukumaran, S., Gopalakrishnan, R.: *Opt. Mater.* **34**, 1946–1953 (2012)
42. Reddy, A.J., Kokila, M.K., Nagabhushana, H., Chakradhar, R.P., Shivakumara, C., Rao, J.L., Nagabhushana, B.M.: *J. Alloys Compd.* **509**, 5349–5355 (2011)
43. Arshad, M., Azam, A., Ahmed, A.S., Mollah, S., Naqvi, A.H.: *J. Alloys Compd.* **509**, 8378–8381 (2011)
44. Joseph, D.P., Venkateswaran, C.: *J. At. Mol. Phys.* (2011)
45. Bouloudenine, M., Viart, N., Colis, S., Kortus, J., Dinia, A.: *Appl. Phys. Lett.* **87**, 052501 (2005)
46. Ullah, R., Dutta, J.: *J. Hazard. Mater.* **156**, 194–200 (2008)
47. Koidl, P.: *Phys. Rev. B.* **15**, 2493 (1977)
48. Muniraja, P., Kumar, K.S., Ramanadha, M., Sudharani, A., Ravi, M., Vijayalakshmi, R.P.: *J. Supercond. Nov. Magn.* **32**, 2175–2183 (2019)
49. Pal, B., Dhara, S., Giri, P.K., Sarkar, D.: *J. Alloys Compd.* **615**, 378–385 (2014)
50. Wojnarowicz, J., Omelchenko, M., Szcztyko, J., Chudoba, T., Gierlotka, S., Majhofer, A., Twardowski, A., Lojkowski, W.: *Crystals.* **8**, 410 (2018)
51. Gao, D., Zhang, Z., Fu, J., Xu, Y., Qi, J., Xue, D.: *J. Appl. Phys.* **105**, 113928 (2009)
52. Xu, L., Zheng, G., Wang, J., Xian, F., Liu, Y.: *Optik.* **127**, 5942–5949 (2016)
53. Godavarti, U., Mote, V.D., Reddy, M.R., Nagaraju, P., Kumar, Y.V., Dasari, K.T., Dasari, M.P.: *Phys. B Condens. Matter.* **553**, 151–160 (2019)

Publisher's note Springer Nature remains neutral with regard to jurisdictional claims in published maps and institutional affiliations.